A novel physisorption model based on mathematical morphology operators preserving exact pore morphology and connectivity

Adam Hammoumi, Maxime Moreaud, Dominique Jeulin, Elsa Jolimaitre, Thibaud Chevalier, Loïc Sorbier, Michaela Klotz, Alexey Novikov

A novel physisorption model based on mathematical morphology operators preserving exact pore morphology and connectivity

Adam Hammoumi[a,*], Maxime Moreaud[a,b], Dominique Jeulin[b], Elsa Jolimaitre[a], Thibaud Chevalier[c], Loïc Sorbier[a], Michaela Klotz[d], Alexey Novikov[d]

[a] *IFP Energies nouvelles, Rond-point de l'échangeur de Solaize BP 3, 69360 Solaize, France*
[b] *MINES ParisTech, PSL-Research University, CMM, Fontainebleau, France*
[c] *IFP Energies nouvelles, 1 et 4 avenue de Bois-Préau, 92852 Rueil-Malmaison, France*
[d] *LSFC Laboratoire de synthèse et fonctionnalisation des céramiques UMR 3080 CNRS/SAINT-GOBAIN CREE, Saint-Gobain Research Provence, 550 avenue Alphonse Jauffret, Cavaillon, France*

Abstract

Complex large models of multi-scale microstructures of porous media do not exist in a manner adequately efficient to render their comprehensive analysis of textural and structural properties possible. The simulation of experimental processes, such as gas adsorption, raises two issues. First, the modeling of these complex materials must be sufficiently realistic. This implies that the numerical twin of the porous material must consider three essential aspects: a spatial structure defining different scales of porosity, comparable textural and structural properties of the real material and irregular pore morphology. Secondly, efficient algorithms must be developed to mimic the quasi-static phase transition behavior of fluids in a realistic manner. The proposed simulation approach allows to handle the physico-chemical phenomena inside complex materials by means of well-established mathematical operators. Morphological operators are used to efficiently mimic processes such as surface adsorption and pore filling. Fluid percolation that provokes phase transition is simulated by labeled connected components. This method relies entirely on morphological and structural operators, which has the advantage of substantially reducing the calculation time compared to that of density functional theory and molecular simulations-based approaches. In contrast to over-simplified models characterized by ideal pore shape and unconnected pores, our approach enables us to calculate the adsorption isotherm of realistic random models where pore morphology and porous network topology are unknown beforehand. We demonstrate that our model succeed in reproducing the adsorption isotherm of two well-known model materials (SBA-15 and KIT-5) and

mesoporous alumina, represented by Cox Boolean models.

Keywords: Gas adsorption, SBA-15, KIT-5, mesoporous alumina, Cox Boolean models

1. Introduction

Pore network structure as well as pore morphology and topology are of paramount importance for several fields, including heterogeneous catalysis and separation by adsorption or membrane processes [13]. In order to reach a thorough comprehension of the interplay between pore network structure and related physico-chemical phenomena, it is mandatory to gain a deep understanding of the obtained results through the characterization techniques of porous materials. This is because the physico-chemical phenomena that occur inside the porous bodies (such as mass transfer, catalytic reactions, capillary effects) are highly impacted by the geometric properties of the pore networks, including pore size distribution, porosity, and connectivity. Over the years, different characterization techniques have been developed to acquire textural properties of pore networks. The most common ones are mercury porosimetry and nitrogen sorption, which consist in measuring the quantity of probe molecules that accumulate in the solid at different fluid phase pressures. The advantage of these techniques is their sensitivity to nearly all the properties cited above. The drawback is that the classical models used to process the experimental data yield approximated or even erroneous results. For example, it is well-known that the Barret-Joyner-Halenda (BJH) model yields two different pore size distributions from the adsorption and desorption branch of the nitrogen isotherm. The first reason for these discrepancies is the complexity of the physico-chemical phenomena occurring inside the pore network. The second reason is the intrinsic complexity of the pore networks of most catalysts and adsorbents. Apart from very particular solids, such as zeolites or meso-structured materials, the size of pores and geometry of catalysts are generally unknown. Also, different levels of porosity can be present in the pore structure, yielding hierarchically organized materials. Recent works dealing with adsorption-induced deformation of mesoporous materials with corrugated cylindrical pores have shown the sensitivity of the adsorption isotherm

*Corresponding author
Email address: adam.hammoumi@ifpen.fr (Adam Hammoumi)

to the geometry of pores [30, 32, 14], which encourages developing models not assuming ideal geometry of pores. The experimental part of the characterization techniques has been extensively advanced in the last decades [47], yet the interpretation and analysis of the obtained results can still be considered as a major challenge [47]. This paper is devoted to the characterization of textural properties of nanoporous materials from a numerical point of view with a focus on gas adsorption. This phenomenon has the advantage of covering the entire nano/mesopore scale [46]. The foundations of our knowledge concerning gas adsorption are based on theoretical models from the early 20th century [20, 5], advances in experimental techniques [10] and numerical models [55, 52, 45] allowing the understanding of underlying phenomena at the pore scale. The most popular gas adsorption porosity analysis models can be grouped within the following families:

- Statistical micro models, allowing the description of physico-chemical phenomena using statistical mechanics, such as density functional theory based approaches and molecular simulation methods. The advantage of these models is that they consider the fluid/fluid and fluid/solid interactions at the molecular level, and can thus simulate in detail the impact of pore shape or adsorption strength [34, 28]. However, they are very time-consuming and therefore limited in terms of computation volume.

- Macroscopic models based on classical thermodynamics, such as the Langmuir or Brunauer, Emmett and Teller (BET) model for adsorption and the Kelvin or Cohan model for capillary condensation. These models can be applied to different pore network geometries, from unconnected pores, as in the well-known BJH model [47, 50], to more complex pore networks, based on interconnected cylinders or spheres [35, 23, 56]. These models are less time-consuming than molecular simulations but cannot represent adequately the disordered pore network geometry of most catalysts.

With the new modeling strategy described in this paper, also based on classical thermodynamics, it is possible to simulate the adsorption behavior of any complex pore network (i.e. no assumption on pore shape or connectivity) in a reasonable amount of time. Our approach is mainly based on correlations, derived from classical pore size analysis methods, between morphological parameters

and physical quantities characterizing the system. Following this path, it is possible to transform the description of quasi-static states of physico-chemical systems, such as phase changes at equilibrium, to a purely geometrical and morphological description of the same phenomena. Mathematical morphology as a theory and technique for the analysis and processing of geometrical structures [48], has been interested since its birth in the characterization of the textural properties of images and volumes of microstructures. For example, G. Matheron in 1967 [37] has shown the possibility of studying the statistical size distribution of a collection of objects by the morphological opening operator. The behavior of several morphological operators, taken individually or in combination, can mimic several physico-chemical phenomena. As our focus is the simulation of gas adsorption, the promise of this work is to deliver tools allowing accurate modeling of gas adsorption and related phenomenon such as multilayer gas adsorption, capillary condensation, thermodynamic hysteresis and gas phase percolation through the simulation of finite size systems instead of infinite ones. In this work, we extend our simulation approach to three digital microstructures of distinct pore network architectures. Pore ordered mesoporous silica SBA-15 [17] and cage-like structure of interconnected pore channels mesoporous silica KIT-5 [58] were reconstructed numerically by uniform lattices of spheres and cylinders. These materials which have been extensively studied from an experimental point of view, are essential for the validation of our model. The fact that their microstructure and its morphological characteristics are known in advance, allows a direct verification of the validity of the model. The versatility of our approach and its independence from any geometrical or morphological constraints, is tested on a multi-scale Boolean model of mesoporous alumina, characterized by random pore morphology and complex pore network. The creation of digital twins of catalytic materials from random microstructure models [53], and their adjustment by numerical models mimicking experimental procedures such as gas adsorption, will eventually contribute to the journey of designing tailor-made solid catalytic materials with specific transport properties.

2. Methods

Previous works relying on morphological and geometrical criteria to simulate gas sorption, or similar phenomena, have shown prominent results in reproducing experimental isotherms, which initially encouraged the core of this research. In contrast to the classical modeling of porous samples by means of simplified pore networks, made of interconnected cylinders representing pores and pore necks, the modeling methodology endorsed by morphological modeling based approaches allows to digitally represent porous media of any pore morphology. Almost all proposed sorption simulation algorithms follow somehow the same pattern, whether it is an interface tracking scheme to fill and empty pores at adsorption and desorption, as in [59], or, by means of morphological operators such as the closing operator by a spherical structuring element [54], the steps involved are similar. Initially, capillary condensation happens in narrow regions which are the corners of pores. Afterwards, when the critical radius given by the Kelvin equation is reached, a sudden filling of the pore occurs. Similarly, desorption follows the inverse path for emptying pores. However, the former methods have their limitations as well. Besides the underlying assumptions regarding the smoothness and energy homogeneity of solid interfaces, the filling and emptying algorithm follows classical schemes, such as the Kelvin equation's based approaches, which are less accurate than density functional theory (DFT) methods. As a consequence of that, phenomena as mono and multilayer adsorption are either not taken account as in [59] or initially imposed [54]. Another major drawback of some of these methods is the non-realistic modeling of these processes, in particular, pore blocking effect which is a major contributor to adsorption hysteresis in hierarchical porous materials. For instance, filling holes primarily to morphological closing without any percolation analysis, presented in [54] is a non realistic description of desorption yielding an inaccurate desorption branch. This work is built on the same macro steps while mimicking in a realistic way the physico-chemical processes to ensure coherent correspondence vis-à-vis both physical processes and experimental results.

2.1. Simulation framework

In what follows, $\mathbb{E}$ refers to a construction space describing spatial phenomena, for instance, a binary microstructure. $\phi(\mathbb{E})$ is the set of interacting objects of the microstructure such as solid, liquid or void phase. A physical process can be seen as a phenomenon that is revealing a certain spatial structure. It can be examined from a mathematical morphology point of view as a family of subsets $\phi(\mathbb{E})$ existing in the space of definition denoted $\mathbb{E}$, which is hosting physical transformations. $\phi(\mathbb{E})$ is a boolean algebra [49]. A description of the phenomenon boils down to the determination of existing relationships between the subsets of $\phi(\mathbb{E})$. Given two subsets X and B belonging to $\phi(\mathbb{E})$, B can help to describe unrecognized patterns of X by the application of morphological transformations [49]. This approach also allows to mimic quasi-static phenomena since B constantly alters the structure of X based on some morphological criteria. That is, B is serving as a structuring element to X. Let the euclidean space $\mathbb{E} = \mathbb{R}^3$ be the space of definition. $X \subset \mathbb{R}^3$ is defined as a set of elements belonging to the binary microstructure. X translated by $u \in E$ is written: $X_u = \{u+x, x \in X\}$. Throughout this paper, the structuring element B denotes a sphere. Morphological transformations are referred to by the symbol ψ:

$$\psi : \mathbb{E} \rightarrow \mathbb{E}$$
$$X \rightarrow \psi(X)$$

Having briefly introduced the mathematical framework, morphological operators are presented hereinafter.

2.1.1. Dilation, erosion and morphological closing

Gas adsorption involves interactions between fluid molecules and solid phase or a solid surface. In particular, gas adsorption is built upon two processes. First, a multilayer adsorption step takes place on the pore walls. This process can be mimicked by a sliding sphere along the solid surface which causes the creation of adsorbed layers. The increase of layer size is equal to the sphere radius.

This operation can be modeled by the morphological dilation [48]:

$$\delta_u(X) = \{u : B_u \cap X \neq \emptyset\} \tag{1}$$

$\delta_u(X)$ is the set of all points u such that structuring element B_u hits X. The opposite operation, causing the solid object to shrink, is given by the morphological erosion:

$$\epsilon_u(X) = \{u : B_u \subset X\} \tag{2}$$

$\epsilon_u(X)$ is the set of all the points u such that B_u is included in X. Second, the condensation of gas due to capillary forces requires a rather more sophisticated operator, capable of modeling sudden filling of pores. The combination of the dilation and erosion operator allows to produce such an operator, called the morphological closing:

$$\phi_u(X) = \epsilon_u \circ \delta_u(X) \tag{3}$$

where the erosion of a dilated object leads to filling pores and narrow spaces. Figure (1) illustrates the three morphological operators on a simple shaped 2D object using a disk structuring element.

2.1.2. Connected components labeling

A pore network is constructed by interconnected open and closed-end pores of different sizes. The shape, size and connectivity to the exterior and to neighbor objects of each pore are important variables affecting undergoing transformations. Percolation of fluid phase through the pore network requires a connected components labeling step. As a matter of fact, this technique holds for the concept of percolation simulation in general [22]. In this configuration, connected pores may behave simultaneously in the same way if they share common properties. In the euclidean space $\mathbb{R}^3$, a connected set X is defined as follows:

$$\forall x \in X \quad \forall y \in X \quad \exists\, \zeta(x, y) \tag{4}$$

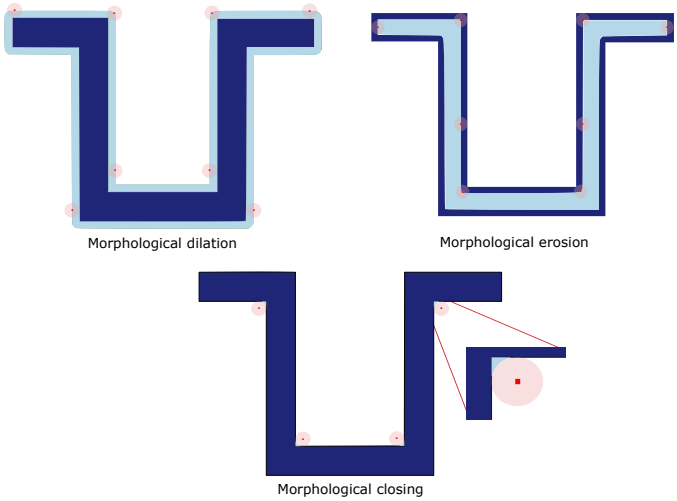

Figure 1: Illustration of the morphological dilation δ, erosion ϵ and closing operation ϕ applied to an arbitrary shape X, in dark blue color. $\delta(X)$ results in the light blue area. In erosion $\epsilon(X)$, the dark blue area is reduced resulting in the light blue area. During morphological closing $\phi(X)$, the disk fills narrow areas.

where $\zeta(x, y)$ is a path included in the set X linking x and y. Size criterion may be added before simulating the percolation phenomenon. As connected component labeling is a widely used operation in pattern recognition, there exists many algorithms addressing this issue quite efficiently [21]. The goal is to map a binary image from its initial form to a set of separate labeled connected components. A connected component is denoted by CC. It can be defined as follows:

$$CC = \{q^{n_1,n_\star}, q^{n_2,n_\star}, q^{n_3,n_\star}, ..., q^{n_m,n_\star}\} \tag{5}$$

By construction, q in Eq.(5) is broadly defined. It can refer to a pore or a pixel/voxel. It should be considered as the basic unbreakable element in the space of definition. $n_{k\in\{1...m\}}$ are the labels initially attributed to each element of the CC. After labeling connected components, each element in CC is labeled by the same label $n_\star$. That is, it is possible to go from an element q to any other element q' by a path which contains only elements of the CC. An example of the connected components labeling operation is illustrated in figure (2). Original image, figure (2a), shows 11 pores with unique labels $1 \rightarrow 11$. The labeling of connected components for this example consists in

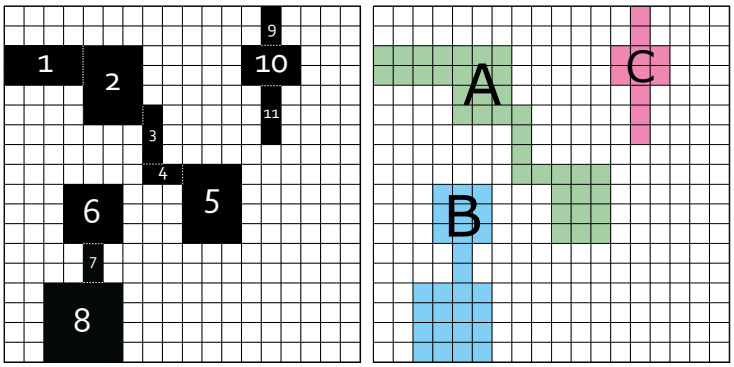

(a) Original image (b) Labeled image

Figure 2: Labeling of connected components in a 2D grid considering a pixel 4-adjacency. (a) original image contains pores in black. (b) labeled image contains classified connected pores A, B and C in different colors.

identifying connected pores which allows to classify three different components; A = $1 \rightarrow 5$, B = $6 \rightarrow 8$ and C = $9 \rightarrow 11$. Subsequently, each component will be uniquely labeled as shown in figure (2b).

2.1.3. Hole filling

Regions of isolated pores, where gas molecules have no path in gas phase to the boundaries, can be extracted by the hole filling morphological operator. The latter is defined as a combination of two operators. A complementary operator considering the microstructure is first applied to extract porous space. Second, connected components in contact with the boundaries of the domain are identified and suppressed. This operation is called border kill. A subsequent step consists in performing union set operation between the output image and initial image. The complementary operator is defined by: $\psi_\beta(X) = \bar{X}$. The border kill operator requires the use of topological boundary concepts and the notion of connected components. The boundary of a subset of a topological space, e.g. in this case, a subset X of the digitized space $\mathbb{Z}^3$, is defined as the closure $\bar{X}$ minus the interior X^o:

$$\partial X := \bar{X} \setminus X^o \tag{6}$$

The border kill operator is defined as follows:

$$\psi_\alpha(X) = \cup_k CC_k \mid \partial X \ \cap \ CC_k = \emptyset \quad \forall k \in \{1, ..., n\} \tag{7}$$

where $CC = \{CC_1, CC_2, ..., CC_n\}$ is the set of the n connected components belonging to X. The hole filling operator writes:

$$\psi_\gamma(X) = (\psi_\alpha \circ \psi_\beta(X)) \cup X \tag{8}$$

This procedure is illustrated in figure (3). Hereafter, the binary microstructure is considered to form a space denoted $\mathbb{I}$. Let $X \subset \phi(\mathbb{I})$ be the porosity phase subset. Its complementary X^c is the subset featuring solid phase.

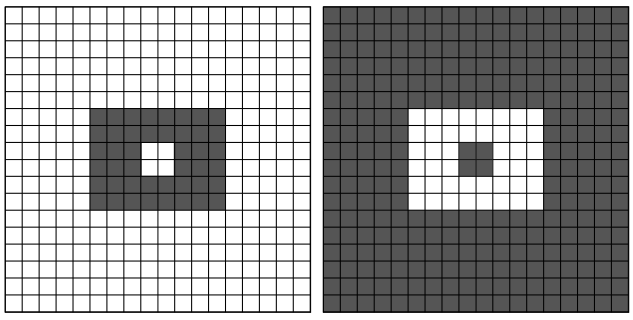

(a) Original image (b) Complementary

(c) Border kill (d) Final image

Figure 3: Steps of the hole filling operation. Image (a) contains in its center the hole to fill. (b) Complementary of the initial image. (c) Removing connected components touching the boundaries of the image. (d) Union of (a) and (c).

2.2. Gas adsorption

Porosity within porous materials is created during synthesis processes [11]. It is defined as the void fraction of empty space within a porous material.

$$\epsilon = \frac{V_v}{V_t} \tag{9}$$

where V_v is the void space and V_t is the total volume of the sample. Depending on the complexity of the material, pore size can be uniform or distributed and the pores of different sizes can be randomly distributed in space or hierarchically organized. Gas adsorption [50] is a powerful and popular technique for the characterisation of porous materials. It allows the evaluation of textural properties such as specific surface area and pore size distribution [7]. For gas adsorption, the minimum analysable pore size depends inherently on the size of the used gas molecule. Most of its analysis procedures consist on methods underpinning correlations between physical and morphological parameters. Kelvin's equation [18] allows a mapping from the physical space, relative gas pressure p/p_0, to the morphological space, fluid curvature radius of the vapor-liquid surface, which is considered as pore radius r in our approximation. The following equation expresses this type of relation:

$$V = Cf(r) \tag{10}$$

where C is a constant including several physical or geometrical properties of the system and V denotes the corresponding fluid volume. In our approach, the morphological operators are the unique tools allowing the simulation of adsorption and capillary condensation. Kelvin and Harkins–Jura equations serve as a mapping between the morphological/geometrical space and the parameters of the physical system. In other words, these equations are used in a post-processing step in order to convert pore radius to p/p_0, which is necessary to compare simulated and experimental adsorption isotherms. For a fixed gas temperature, an adsorption branch is obtained by gradually increasing the relative pressure to the saturation pressure, and a desorption branch by decreasing the relative pressure from the saturation pressure to zero. Usually the adsorption and desorption branch follow different paths, which gives rise to hysteresis. In what follows, the modeling of this phenomenon is

discussed in details.

2.3. Simulation Model

The objective of our model is to mimic the behavior of fluid during gas adsorption. A typical example of adsorption isotherm is illustrated in figure (4). The set of tools developed in this section will allow to calculate the adsorption isotherm for a wide range of microstructures for which no simplifying assumptions on the pore geometry and pore network are imposed.

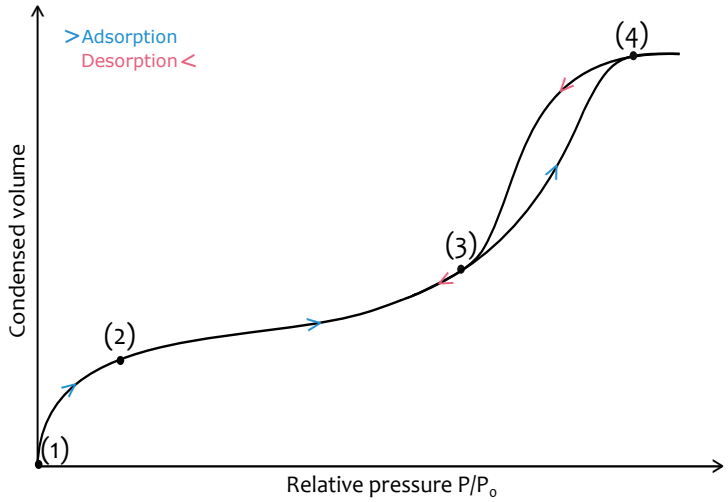

Figure 4: A schematic representation of the various steps involved in the process of gas adsorption. (1) monolayer adsorption. (2) multilayer adsorption. (3) capillary condensation. (4) capillary evaporation.

2.3.1. Notations

The binary microstructure $\mathbb{I}$ is constructed as the space of binary abstract pore and solid objects. This representation allows an abstract and generalizable formulation for the phenomena discussed in this paper. However, the practical representation is that of the digitized space $\mathbb{Z}^3$. The porosity phase X is evolving with respect to pore radius r. It is defined as $X = \cup_r X_r$. Pores are identified by their inter-connectivity. In particular, they are located through the connected components operator defined in (Eq.5). The set of connected components belonging to X_r is denoted CC_r. The modeling of gas adsorption is based on two parameters. The first is pore radius r, whereas the second, denoted λ, defines pores connected to the outside. For an arbitrary set $Y \subset X$, we denote $Y_{r_\geq}$ and $Y_{r_\leq}$

as the set of elements having radius value exceeding (or equal) and limited (or equal) by reference value r, respectively. The subset of Y respecting some radius criterion $r_\star$ and assembling connected elements to the exterior is referred to by $Y^{\lambda}_{r_\star}$.

2.3.2. Nitrogen adsorption

When a porous medium is placed in a vapour atmosphere with gradual increase of gas pressure, a spontaneous process, consisting in the adsorption of gas molecules on the pore walls, is triggered. A monolayer of one gas molecule thick is first formed as a consequence of the coverage of adsorbed molecules. Subsquently, the begining of multilayer stacking of the molecules is caused by increasing pressure. According to the calculation scheme of the BJH method [46], which is based on a discrete analysis of the adsorption and desorption branch, relative pressure intervals, or pore radius values in this case, are considered. For each pore radius, the quantity of adsorbed gas comes from two phenomena. First, the increase of the thickness of adsorbed layer for a certain pore size or relative pressure range. Second, from the capillary condensation of gas, i.e. the phenomenon by which a gas in a capillary pore condenses to a liquid-like phase at gas pressure p below the saturation pressure p_0 [50]. This process can be formulated as follows:

$$\Delta V_{ads} = \Delta t \cdot A + V_{r_p} \tag{11}$$

where ΔV_{ads} denotes the total condensed volume of gas at radius value r_p. Multilayer pore filling is expressed by the product of the film thickness and accessible surface area $\Delta t \cdot A$, whereas V_{r_p} denotes the volume condensed throughout capillary condensation. The Harkins–Jura equation [19] for N_2 can be used to calculate the film statistical thickness t:

$$t = 0.1\left[\frac{13.99}{0.034 - 0.4343\,\log(p/p_0)}\right]^{0.5} \tag{12}$$

While our model relies on a morphological approach based on the pore radius, (Eq.12) describes the dependence of the film thickness to gas relative pressure. The Kelvin's equation is a key tool for pore size analysis, in particular for mesopore analysis [51]. It has provided a relationship between

the capillary radius and saturated vapor pressure of adsorbate on spherical meniscus at capillary condensation. However, the original model fails to take into account the adsorbed film thickness formed on pore walls. This issue can be solved by the Derjaguin–Broekhoff–de Boer (DBdB) theory [45, 31], which, in addition to the capillary gas pressure, considers the disjoining pressure of liquid film in describing adsorption. Since our model is interested only in reproducing experimental adsorption curves analyzed without calculating solid-fluid interactions, the disjoining pressure is omitted. In this case, the DBdB equation reduces to the Cohan-Kelvin equation [57]. Moreover, the DbdB approach is only valid for a thermodynamically isolated system and requires the calculation of the Minskowski invariants of the pore. This is not possible in a sufficiently accurate way on numerical volumes, in particular for the Gaussian curvature integral [33, 43]. The Cohan-Kelvin is a modified Kelvin's equation describing capillary condensation with consideration of adsorbed film for an open-ended cylindrical pore. According to this model, the meniscus between the adsorbed film and vapor is cylindrical at capillary condensation for an infinite cylindrical pore:

$$\ln(p/p_0) = \frac{-\gamma V_m}{RT(r-t)} \tag{13}$$

According to the same model, desorption is described with the formation of a hemispherical meniscus between the condensed fluid and vapor:

$$\ln(p/p_0) = \frac{-2\gamma V_m}{RT(r-t)} \tag{14}$$

where p is the vapor pressure, p_0 saturated vapor pressure, γ vapor-liquid surface tension, V_m molar liquid volume, R gas constant and T gas temperature (77 K for N_2). These parameters are usually considered to be constant under some assumptions. r is the pore radius. t is the adsorbed multilayer film which can be obtained from (Eq.12). While keeping in mind the underlying assumptions behind the Cohan's model, (Eq.13) and (Eq.14) are used in our simulation framework to generate adsorption isotherms in terms of relative vapor pressure p/p_0 instead of pore radius r. Two types of gas behavior are therefore considered. The first one refers to a progressive gas-liquid phase transition that occurs over the area of pores in a layered form. This process can be simulated using the

dilation operator described in (Eq.1). One dilation operation over the original microstructure with structuring element B_t as a sphere of radius t, corresponds to monolayer adsorption. Assuming that the sphere radius t is equal to the film thickness, multiple use of the dilation operator with increasing t, given in (Eq.12), allows simulating multilayer adsorption:

$$\delta_{t_n} \circ \delta_{t_{n-1}}(X) \qquad n \in \{1, ..., N\} \tag{15}$$

where δ_{t_n} is the dilation operation by a sphere with radius t_n and $\delta_{t_0}(X) = X$. The number of adsorption layers is reflected by the range of n and t_{n-1} is the film thickness for $n-1$. Note that for the first dilation operation δ_{t_1}, the sphere radius t_1 is equal to the radius of one N_2 molecule (roughly 0.15 nm, which imposes a resolution of 1 voxel = 0.15 nm in a 3D discrete grid, yielding an accuracy of one layer at a time). If the resolution R is imposed and $R > 0.15$ nm, then the precision decreases by a factor of $R/0.15$. For example, for an imposed resolution of 1 voxel = 0.3 nm, two layers will be filled at a time. Capillary condensation exhibits a different kind of gas behavior that is characterized by sudden gas condensation. This process is achieved by using the morphological closing operator. The capillary condensation operator writes:

$$\phi_{r_n} \circ \delta_{t_n}(X) \tag{16}$$

where ϕ_{r_n} is the closing operator (Eq.3) provided with structuring element of increasing size $r_n = r + t_n$, such that r is calculated from (Eq.13) and $n \in \{1, ..., N\}$. The latter fills narrow regions and pore space in proportion to r_n until all pore space is filled. Figure (4) may be broken down to path (1) $\rightarrow$ (2) $\rightarrow$ (3) $\rightarrow$ (4), corresponding to adsorption and its inverse, desorption. The values of condensed vapor volume are plotted against their related increasing relative pressures p/p_0. Another representation of the adsorption isotherm in the context of morphological simulation is given by considering the number of voxels $|.|$ resulting from morphological dilation and closing as condensed volume. The function allowing to compute the number of elements contained in the

transformed porosity phase, i.e. condensed volume, is given by:

$$G_n(X) = \begin{cases} \left|\delta_{t_n}(X) - \delta_{t_{n-1}}(X)\right| \\ \left|\phi_{r_n} \circ \delta_{t_n}(X) - \phi_{r_{n-1}} \circ \delta_{t_{n-1}}(X)\right| \\ 1 \leq n \leq N \end{cases} \tag{17}$$

Traditionally, the measurement of granulometric functions, allowing the computation of size distribution of grains or pores in binary images, is done by the opening morphological operator, as introduced in [37, 38]. However, it is not the case here, since both the closing and the dilation operators violate the anti-extensivity axiom (i.e, $\forall\ X \subseteq I,\quad \psi(X) \subseteq X$). $G_n(X)$ is dependent on pore radius r and film thickness t. That is, the initial porosity set X will be continuously transformed by morphological operators which yields to subsets $\{X_{r_n} \mid 1 \leq n \leq N\}$. The adsorption curve is cumulative:

$$\begin{cases} A_0(X) \quad = 0 \\ A_{n+1}(X) = A_n(X) + G_{n+1}(X) \\ n \in \{0, .., N-1\} \end{cases} \tag{18}$$

$A(X)$ is to be considered as a sequence of elements in the ascending order. These elements refer to the amount of the condensed vapor. Following this approach, a new isotherm curve parameterized by the pair (number of voxels, pore radius) is obtained from which the pore size distribution can be deduced straightforwardly. Figure (5) illustrates the different steps of capillary condensation for a system of pores having radius in range $[1, 4]$ voxels. It is shown that the only criterion for a pore to be filled is pore radius.

2.3.3. Desorption

Adsorption systems often reveal associated hysteresis to the capillary condensation process [50]. This phenomenon carries valuable information regarding the internal structure of porosity and topology of pores. Correlations between textural information and some of the most common hysteresis loops are given by the IUPAC report [51]. Hysteresis occurs at different scales of porosity. That is, hysteresis may occur at the level of one pore or at the level of pore network. A modeling procedure taking into account multi-scale hysteresis causes by means of morphological parameters

is required. At the pore level, hysteresis is principally triggered by delayed vapor-liquid transition, mainly due to adsorption metastability and to obstructed nucleation of liquid bridges [50]. At the pore network level, hysteresis is due to the pore blocking effect as well [50]. The latter describes the obstruction of big pores by smaller ones, their evaporation is no longer pressure dependent but delayed until the smaller pores are evaporated. This phenomenon alters the order of desorption process, leading to hysteresis. The onset of desorption is the endpoint of adsorption. In spite of their divergence caused by hysteresis, their boundary conditions are maintained identical. Our modeling strategy for desorption and hysteresis is the following. For cylindrical pores, Cohan's model is used to take into account the hemispherical meniscus between the adsorbed film and vapor during desorption, which allows to mimic delayed evaporation. The modeling of pore blocking effect in complex pore networks is done through a sequence of steps. First, connected components to the boundaries of the microstructure domain are identified and labeled, then grouped by classes according to their radius so that future actions can be applied on a set of separated pores of the same class. Second, a percolation operator is applied on these elements contained in each X_{r_n}. The operation is applied step-by-step on the basis of radius values until the end of the process. For pore blocking modeling:

$$CC^{\lambda}_{r_{n\geq}} = \left\{ \underbrace{\forall\, CC_a \subset CC_{r_{n\geq}}}_{\text{radius criterion}} \;\middle|\; \underbrace{CC_a \cap \partial\mathbb{I}_f \neq \emptyset}_{\text{condition } \lambda} \right\} \tag{19}$$

$CC^{\lambda}_{r_{n\geq}}$ is the set of the connected components verifying radius criterion $r_n \geq$ and having contact with the exterior according to condition λ. $\partial\mathbb{I}_f$ denotes the boundaries of the binary microstructure domain. The pore percolation operator, when applied to X, is responsible for extracting the elements of (Eq.19):

$$P_n(X) = CC^{\lambda}_{r_{n\geq}} \tag{20}$$

Figure (5) summarizes this process. Three CC can be identified. Starting from maximum radius value, it is shown that large pores in contact with the boundaries of the domain evaporate first. It is noticed as well that although pore (R = 4) forms one single CC with smaller pores, it is the only one to be evaporated. At the next step, the evaporation is not occurring since pore (R = 3) is obstructed by smaller pores that are in contact with the vapor phase. Afterwards, pore (R = 2) evaporates when

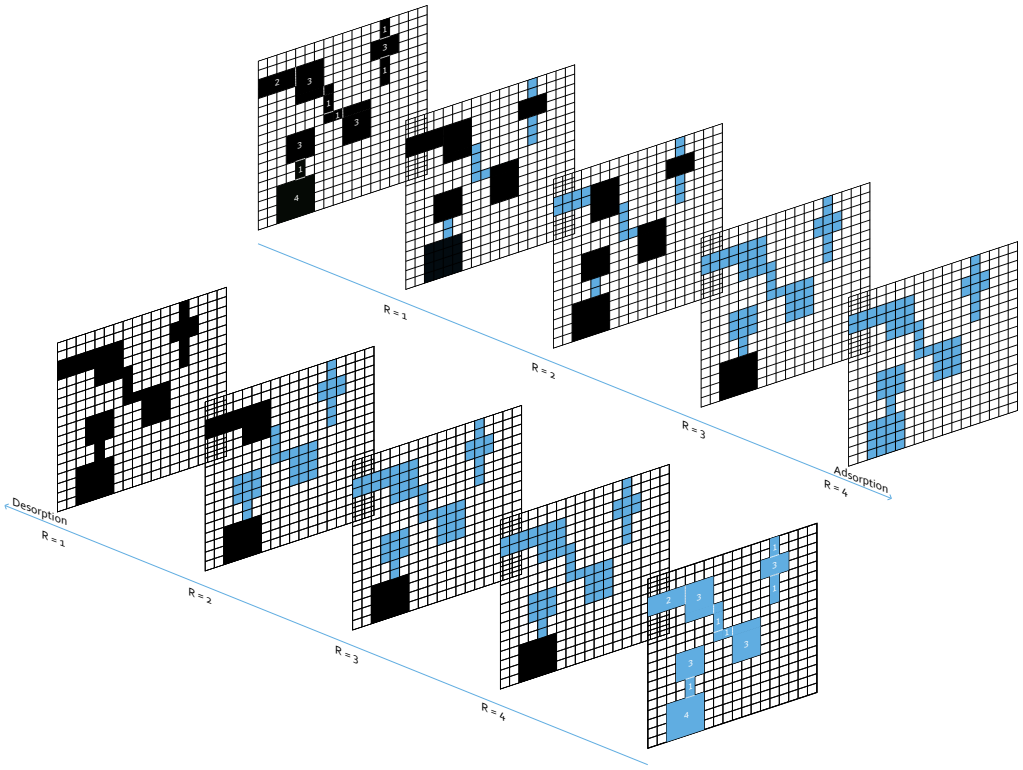

Figure 5: Illustration of adsorption (on top) and desorption (on bottom) for a system of pores with radius in range [1,4]. Monolayer and multilayer adsorption are not illustrated. Void phase is represented by black color and condensed liquid phase is represented by blue color. Hysteresis starts at R = 3 because of the obstruction of pores with radius (R = 3) by smaller pores during desorption.

the radius criterion is reached. The λ condition is verified as well. The same computation scheme is maintained for the rest of pores until total evaporation occurs at R = 1. The desorption operator writes:

$$W_{r_n}(X) = \left|G_N(X) - P_n(X)\right| \quad n \in \{N, .., 1\} \tag{21}$$

where $G_N = W_{r_1}$ and $G_1 = W_{r_N}$.

2.4. Boolean and Cox Boolean models

2.4.1. Boolean models

A porous material can be regarded as a set A, union of uniformly distributed particles embedded in a matrix A^c. The simulation of such two-phase material can be done through a random closed

set modeling [48, 37, 24, 40]. For a random closed set A, the latter provides a full characterization from a probabilistic point of view by its Choquet Capacity $T(K)$:

$$T(K) = P(K \cap A \neq \emptyset) = 1 \; - \; P(K \subset A^c) \tag{22}$$

The Choquet capacity is the probability for the deterministic compact set K to hit the random set A. (Eq.22) can be used for the identification of a model by determining its intrinsic properties such as the volume fraction (considering K a point) and covariance (considering K a bi-point).
The first intuition behind Boolean models is a space implantation of grains, which are independent of each other, whereas having the same stochastic properties, namely a common spatial law. Subsequently, the Boolean model is constructed by the union of the grains [37]. The process of constructing a Boolean model is the following: consider a spatial distribution of random grains A' with their centers x_k located according to a Poisson point process with intensity θ (average number of points per unit volume):

$$A = \cup A'_{x_k} \tag{23}$$

The volume fraction V_v occupied by the grains of the material depends on the average volume $\overline{V}$ of the primary grains and on the intensity θ:

$$1 - V_v = 1 - \exp(-\theta \overline{V}(A')) \tag{24}$$

Boolean models allow the generation of one-scale models of microstructures. They were extensively used in the past for many applications. Among others, early work [3] conducted analytical estimations of the percolation threshold for materials on the basis of Boolean models. Regarding the same topic, it was shown that the percolation threshold can be as well estimated by means of simulations of the Boolean model generated microstructure [27].

2.4.2. Cox Boolean models

The spatial representation of a two scale porous material is a superposition of two distinct scales of void. One reason is the existence of very dense areas, populated by grains where the void between

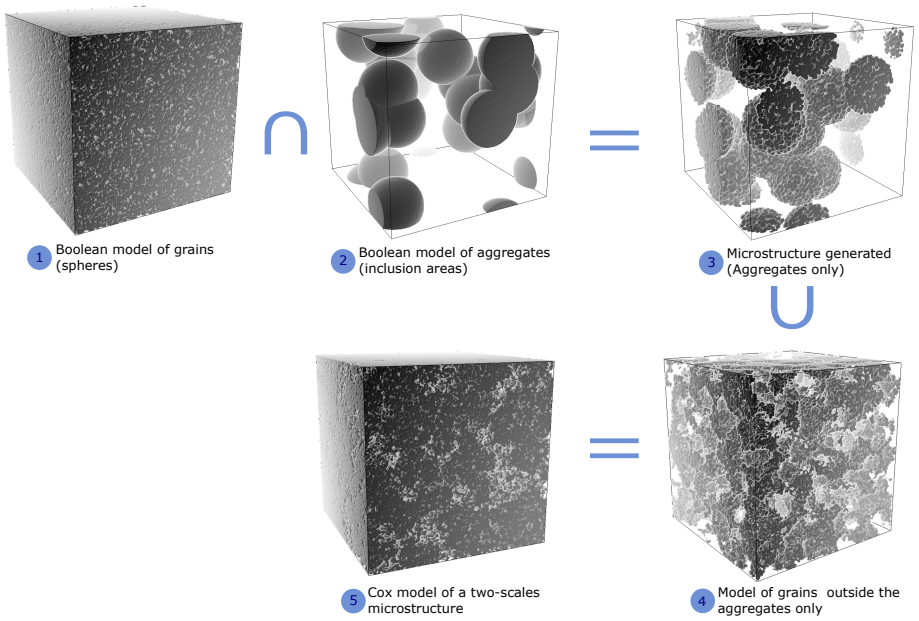

Figure 6: The several steps involved in the Cox Boolean models. Complex microstructures (step 5) are obtained by combining different Boolean models (steps 1,2), and (steps 3,4). The models of generated microstructures are binary and contain two phases (solid in black and void in white).

them represents the first scale of porosity. On the other hand, provided that the grains form the aggregates, larger void, located between the aggregates represents the second scale of porosity. Cox Boolean models [27, 40, 26, 25] are defined by using an intensity $\theta(x)$ not any more constant in space. If $\theta(x)$ is a realization of a positive random function, the point process becomes a doubly stochastic point process called a Cox process [8]. For instance, aggregates may be generated by means of a Boolean model of spheres A_2 with large diameters $d_2 > d_1$. A second Boolean model of spheres A_1 with diameter d_1 and centers generated by a Poisson point process located inside A_2 produces a two-scale Cox Boolean model of spheres. Following this approach, the porosity of a multi-scale model can be controlled by means of basic set operations on Boolean models. Moreover, in Cox Boolean models, the morphology of grains is preserved. Figure (6) summarizes the Cox Boolean modeling process.

3. Results and discussion

In our approach, lattices as uniform tilings by cylinders and spheres were used to represent model materials SBA-15 and KIT-5, as shown in figure (7). Details about the preparation and characterization of the real materials is given in the supplementary information file. Cox Boolean models were used to model mesoporous alumina as shown in figure (7). The adsorbed fluid field incorporate two fields. The first one can be assimilated by the dilation operation of a sphere of radius t_n given by (Eq.1), mimicking the statistical growing thickness t representing monolayer and multilayer adsorption. The second field is given by a closing operation of a sphere of radius r rendering the capillary condensation. At iteration n, all voxels encompassed in spheres of radius t_n and $r_n = r + t_n$, that belong to porosity phase will be considered as adsorbed fluid. Iteratively, this process continues for all accessible pore sites until all the voxels of the pore network have been visited. All simulations were performed using a personal computer (CPU: intel core i7 2.6 GHz, RAM: 16 GB). On average, our N_2 sorption simulation algorithm requires about 40 min for volumes of 250 nm^3. With regard to the experimental isotherms of model materials SBA-15 and KIT-5, simulated isotherms were generated on the basis of numerical model materials shown in figure (7). A comparison between simulated and experimental isotherms is given in figure (8). Hereinafter, we give a point by point analysis of the obtained results.

SBA-15

SBA-15 is characterized by excellent structural order and a narrow distribution of mesopores [16] as exhibited by a steep capillary condensation step at high relative pressures in the experimental isotherm, figure (8). Another essential feature of the SBA-15 material is a pronounced sorption hysteresis. This brings us to the global question of hysteresis in microstructures with simple topology, consisting of straight, disconnected pores. For this type of microstructures, the interpretation of hysteresis is yet to be entirely resolved [6]. One of the possibilities that explains the occurrence of hysteresis is the existence of narrow sections inside the pores, which was first introduced in [12]. The latter can be conceptualized as the roughness of the material, i.e., surface imperfections on the pore walls. The modeling of this phenomenon requires distorting the internal diameter of

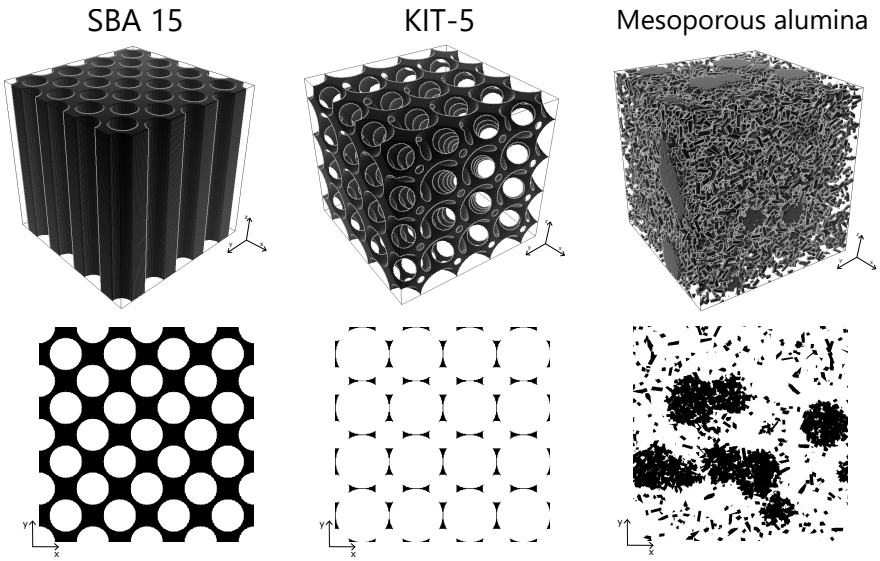

Figure 7: (Top row) 3D models of model materials considered in this work and mesoporous alumina. SBA-15 and KIT-5 are highly ordered microstructures in the range of mesopore, made of cylinders and spheres shaped pores. Mesoporous alumina is modeled by a Cox Boolean model of platelets. (Bottom row) 2D corresponding slices of the 3D models in top row.

the pore. In this case, the evaporation of the pore will be delayed by the largest percolating section of the pore. With reference to this possibility, several works have proposed a model of cylindrical pore with constrictions [6, 4] that have been observed experimentally [15]. A second interpretation, particularly relevant in the case of smooth pore walls, is the dependence of hysteresis upon pore length. For instance, references [16, 42] report that pore length plays an important role in determining the shape of sorption hysteresis loop in the case of finite length cylindrical pores. In particular, Grand Canonical Monte Carlo (GCMC) based simulation of argon adsorption at 87.3 K in cylindrical pores [16] has shown that reversible isotherm is observed for extremely short (L = 4 nm) pores, whereas for longer pores, large hysteresis occurs. Its shift to the left of the desorption curve is proportional to the increase in pore length. Similar work modeling large systems by using the three-dimensional Lenz-Ising model has studied the impact of the pore length on the hysteresis loop. Analogous conclusions were reported in [2] confirming that the maximum hysteresis loop width is found in the case of infinite pores, wherein finite pores exhibit narrower hysteresis. The

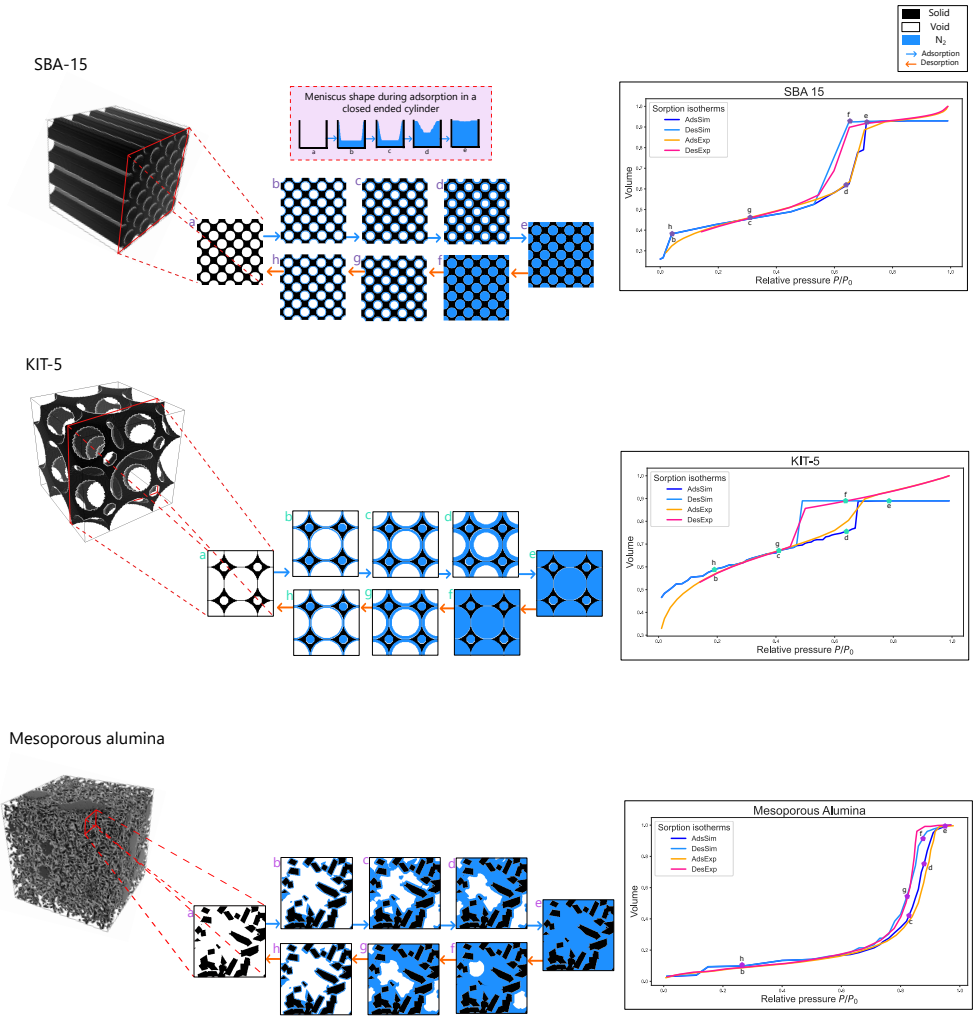

Figure 8: Experimental and simulated N_2 sorption isotherms for the three materials (SBA-15, KIT-5 and mesoporous alumina). For each material, adsorption and desorption steps are illustrated by images from our simulations.

Cohan's model allows to obtain a hysteresis loop due to different meniscus shape during adsorption and desorption. However, this approach, which is widely used to model equilibrium phase transitions, is based on the assumption that cylindrical pores are infinitely long [41, 44]. The adsorption branch is located at a higher pressure than that of the desorption branch with a fixed gap given by the ratio of pore radius during adsorption and desorption $r_{ads}/r_{des} = 2$. By comparing the result

of this approach with experimental isotherms of SBA-15, the found numerical isotherm exhibits larger hysteresis. A direct inference from the latter observation, coupled with the arguments from the above, raise concerns about the use of the Cohan's model to describe hysteresis for finite cylindrical pores that are more likely to be an accurate representation of real SBA-15 like materials. We propose a correction factor calculated from experimental reference data and which allows to find the right gap between the two branches. Assuming that hysteresis depends on the pore length, the correction factor can be calculated through an empirical model [16, 42]:

$$K_c = \frac{1}{0.5 + \frac{e^{-L/m}}{2}} \tag{25}$$

where L is the length of the pore and m is a constant factor allowing to find the correct K_c by comparing simulated isotherm against experimental isotherm. Figure (9) shows the hysteresis loop calculated for four cylindrical pores of radius $r = 4$ nm while having different pore length (L = 5, 25, 50 nm and infinity). Feeding the correct length of pores into the model and adjusting m in accordance with experimental isotherm allows to find the right gap between the adsorption and desorption branch. Our modeling is based on the reference [36], indicating reliably the length, the diameter and the technique used (N_2 adsorption). In accordance with experimental observation, we find $K_c = r_{\text{ads}}/r_{\text{des}} = 1.41$. The simulated isotherm in figure (8), shows good agreement with its experimental equivalent in the hysteresis region. The fact that the length of SBA-15 pores from our TEM images (in supplementary information file) is found to be of the same order of magnitude as the length of the SBA-15, on which the model was calibrated, confirms our findings. It is shown that the trend of the multilayer adsorption is respected. However, there may be some inconsistencies compared to the experimental isotherm. The latter are related to the experimental model of Harkins-Jura (Eq.12) on which the calculation is based. The calculated curve is scaled with respect to the experimental curve. Real SBA-15 contains large mesopores outside the cylinders pores, giving rise to a gradual filling of these regions at large pressures. This part is not taken into account in our modeling, hence the stop of the simulated curve at volume $\simeq 0.9$. Best agreement with reference to the experimental isotherm was found for a narrow pore size distribution ($\simeq$ 14 % relative

standard deviation). The pore network is made of cylinders of radius in range [2.8, 3.4] nm, which is coherent with the BJH adsorption average pore radius (= 2.85 nm) given in the supplementary information file. This result identifies type IV(a) isotherm as well as an H1 hysteresis loop, which is correspondent to the expected features of the SBA-15 material.

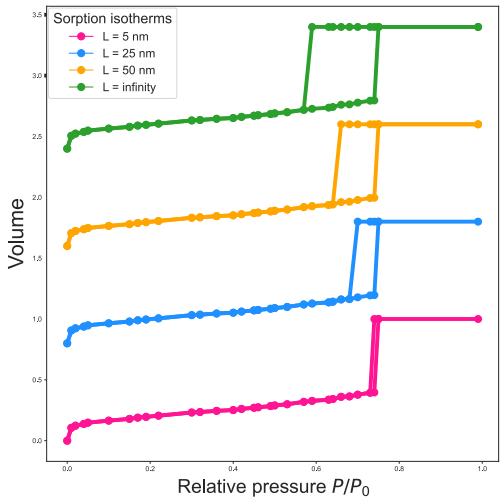

Figure 9: Simulation of N_2 adsorption at 77 K in cylinders pores of 4 nm radius having different lengths. The isotherms of the 25, 50 nm and infinity are shifted up by 0.8, 1.6 and 2.4, respectively.

KIT-5

KIT-5 has a face-centered-cubic Fm3m symmetry structure with interconnected pore channels [29, 9]. The cage-like structure is modeled by a spatial repeatability of a basic mesh. The latter is characterized by its size W, the radius of spherical pores r_s and the spacing between pores S_p (> 0 if there is no overlapping and ≤ 0 otherwise) . Tuning these parameters allows to obtain different accessible pore volume and surface area values. The interconnectivity of pores, controlled by S_p in our model, plays a major role in defining the shape of the adsorption-desorption isotherm. In contrast to the SBA-15 material, which has no network impact on the hysteresis loop, KIT-5 material can have several neck sizes according to the ink-bottle pore model, which directly controls the shape and width of the hysteresis loop. The reference experimental isotherm, shown in figure (8) is of type IV with a broad H2 hysteresis loop. At high relative pressure ($p/p_0 \simeq 0.7$), a sharp

increase in the adsorption curve is indicative of large uniform cage-type pores. Similar to SBA-15 numerical isotherm, the calculated curve has been scaled with respect to the experimental isotherm (accessible volume stops at approximately 0.9). In our approach, hysteresis is due to two distinct phenomena. On the one hand, Cohan's model is applied, as the pores are assumed to be cylindrical. On the other hand, pore blocking effect is pronounced as a consequence of the interconnectivity of pores. It was found that the combination of these two factors along with the parameters ($r_s = 3.1$ nm, $S_p = -1.4$ nm) yield numerical isotherm which is in good qualitative agreement with the experimental reference. Note that r_s is close to the BJH adsorption average pore radius ($\simeq 2.55$ nm), given in the supplementary information file.

Mesoporous alumina

Mesoporous alumina is represented by a Cox Boolean model in a 3D voxel array. The aggregates and platelets are randomly packed following Cox's law according to the process explained in section on Boolean and Cox Boolean models. Each voxel is either classified as a pore space (voxel value = 255) or material space (voxel value = 0). Edge effects are minimized by employing periodic boundary conditions, such that if a part of a platelet is extended outside the cell edge, it gets wrapped around the other side. The parameters of a Cox model are related to the total porosity ϵ by the relation:

$$P_b(1 - P_s) + P_a P_s \simeq 1 - \epsilon \tag{26}$$

where P_s is the volume fraction of the aggregates inside the matrix and P_a, P_b are the volume fractions of the grains inside and outside the aggregates, respectively. Grains and aggregates are modeled by platelets and spheres, respectively. The parameters used for mesoporous alumina were directly taken from reference [53]. The shape of grains is assumed to be parallelepipedic. The dimensions of platelets were identified using an inverse problem approach with L2-normalization of the correlation function on the basis of TEM image of sliced sample [54]. The parameters used for platelets are: L (length) = 14.3 nm, H (height) = 4.4 nm and T (thickness) = 3.3 nm. The sharp increase in the adsorption branch at high relative pressures shown in figure (8) is featuring narrow pore size distribution. The proportion of small pores is relatively small compared to larger pores

which suggests a dominance of inter-aggregates void. Therefore, the quantity of grains inside the aggregates P_a must be larger than the quantity of grains outside the aggregates P_b (reference [53] reports a low volume fraction of aggregates $P_s = 0.2$). This observation is very much reversed when the aggregates are present in a more important proportion. For mesoporous alumina, there are two possible factors causing the appearance of hysteresis. First, pore blocking which is present but to a lesser extent compared to KIT-5 material. In contrast to the latter, the majority of large pores are already percolating with the outside and only a few are blocked by smaller pores. If only the pore-blocking effect is taken into account, we numerically obtain a narrower hysteresis than the experimental reference. The second possibility relies in introducing the pore-length correction factor (Eq. 25) to adjust the gap between the adsorption and desorption branch. As seen before, the value of K_c is related to the pore length (i.e. $K_c = 1$ for closed cylinders and $K_c = 2$ for infinitely long open cylinders). However, for an isolated pore of given geometry, K_c (or rather r_{ads}/r_{des}) can be related to the pore shape as well [39]. In our case, K_c is optimized in a way that it represents the average K_c for all pore shapes encountered in the Cox Boolean Model. Best agreement with reference to the experimental isotherm curve is found for $P_a = 0.95$, $P_b = 0.12$ and $K_c = 1.22$.

4. Conclusion

A modeling approach based on morphological operators has been developed to efficiently calculate gas adsorption isotherm. Mathematical morphology operators have allowed to mimic the quasi-static phase transition behavior of fluid during gas adsorption. A percolation algorithm was deployed to handle pore blocking during desorption. All operators were written under a generic mathematical formalism, specifically developed for this study with the potential to build on it for other modeling applications. Our model has been successfully applied to network-scale simulations of nitrogen adsorption at 77 K in 3D lattices of uniform tilings and Cox Boolean models, to simulate SBA-15, KIT-5 materials and mesoporous alumina, respectively. While Cox model was used to illustrate that the model can be extended to random geometries of pores. The latter is not mandatory for our model, which is by no means restricted to Cox models and can be applied to any 3D model of a binary microstructure. A case-by-case analysis was provided with a focus on

the hysteresis region of the simulated isotherm. Comparisons against experimental isotherms allowed to identify a novel parameter to be added to our model. SBA-15 experimental isotherm has shown inconsistency with respect to the Cohan's model. This result has led to the adding of a new parameter considering the length of pores. A parameter that can be generalized for different types of microstructures. For ordered mesoporous materials such as SBA-15, pore length is a physical parameter that can be measured by microscopy techniques such as SEM. For disordered materials such as alumina or silica this parameter has to be estimated. If this is done for several samples of the same type of material, and very close values are obtained, then an average value can be used thereafter, allowing predicting the isotherms for all materials of the same family where the experimental curve is unknown. The results of model materials have revealed both type IV(a) isotherm and H1, H2 hysteresis loops for SBA-15 and KIT-5, respectively. These results are in good qualitative agreement with experimental data. Mesoporous alumina experimental isotherm was successfully reproduced by our method. Our result of simulation has largely exceeded in precision the result previously found in reference [53]. Moreover, the computation time for large pore networks was found reasonable as discussed in section on Results and discussion. Another line of research would be the use of the same formalism for the development of algorithms for the simulation of mercury intrusion and NMR cryoporometry. The interested reader can find the N_2 adsorption simulation code on the open access software "plug im!" [1]. Microstructures in figures (6, 7, 8) were generated using the same software.

Appendix A.

The following file is available free of charge.

Appendix: XRD, TEM and Nitrogen physisorption characterization results of SBA-15 and KIT-5.

References

[1] "plug im!" an open access and customizable software for signal and image processing, 2021. URL: https://www.plugim.fr.

[2] Altamirano, M.B., Cordero, S., López-Esparza, R., Pérez, E., Goicochea, A.G., 2015. Importance of pore length and geometry in the adsorption/desorption process: a molecular simulation study. Molecular Physics 113, 3849–3853. doi:10.1080/00268976.2015.1070927.

[3] Balberg, I., Anderson, C.H., Alexander, S., Wagner, N., 1984. Excluded volume and its relation to the onset of percolation. Phys. Rev. B 30, 3933–3943. doi:10.1103/PhysRevB.30.3933.

[4] Ball, P.C., Evans, R., 1989. Temperature dependence of gas adsorption on a mesoporous solid: capillary criticality and hysteresis. Langmuir 5, 714–723. doi:10.1021/la00087a026.

[5] Broekhoff, J., de Boer, J., 1967. Studies on pore systems in catalysts: IX. calculation of pore distributions from the adsorption branch of nitrogen sorption isotherms in the case of open cylindrical pores a. fundamental equations. Journal of Catalysis 9, 8–14. doi:https://doi.org/10.1016/0021-9517(67)90174-1.

[6] Bruschi, L., Mistura, G., Nguyen, P.T.M., Do, D.D., Nicholson, D., Park, S.J., Lee, W., 2015. Adsorption in alumina pores open at one and at both ends. Nanoscale 7, 2587–2596. doi:10.1039/C4NR06469K.

[7] Coasne, B., Galarneau, A., Pellenq, R.J.M., Di Renzo, F., 2013. Adsorption, intrusion and freezing in porous silica: the view from the nanoscale. Chem. Soc. Rev. 42, 4141–4171. doi:10.1039/C2CS35384A.

[8] Cox, D.R., 1955. Some statistical methods connected with series of events. Journal of the Royal Statistical Society: Series B (Methodological) 17, 129–157. doi:https://doi.org/10.1111/j.2517-6161.1955.tb00188.x.

[9] Deka, J.R., Lin, Y.H., Kao, H.M., 2014. Ordered cubic mesoporous silica KIT-5 functionalized with carboxylic acid groups for dye removal. RSC Adv. 4, 49061–49069. doi:10.1039/C4RA08819K.

[10] Espinal, L., 2012a. Porosity and its measurement. Characterization of Materials , 1–10.

[11] Espinal, L., 2012b. Porosity and Its Measurement. American Cancer Society. pp. 1–10. doi:10.1002/0471266965.com129.

[12] Everett, D., 1988. Pore systems and their characteristics, in: Unger, K., Rouquerol, J., Sing, K., Kral, H. (Eds.), Characterization of Porous Solids. Elsevier. volume 39 of *Studies in Surface Science and Catalysis*, pp. 1–21. doi:https://doi.org/10.1016/S0167-2991(09)60726-6.

[13] Fechete, I., Wang, Y., Védrine, J.C., 2012. The past, present and future of heterogeneous catalysis. Catalysis Today 189, 2–27. doi:https://doi.org/10.1016/j.cattod.2012.04.003. catalytic Materials for Energy: Past, Present and Future.

[14] Gommes, C.J., 2012. Adsorption, capillary bridge formation, and cavitation in sba-15 corrugated mesopores: A derjaguin–broekhoff–de boer analysis. Langmuir 28, 5101–5115. doi:10.1021/la2051228. pMID: 22324828.

[15] Gommes, C.J., Friedrich, H., Wolters, M., Jongh, P.E.d., Jong, K.P.d., 2009. Quantitative characterization of pore corrugation in ordered mesoporous materials using image analysis of electron tomograms. Chemistry of Materials 21, 1311–1317. doi:10.1021/cm803092c.

[16] Guillet-Nicolas, R., Ahmad, R., Cychosz, K.A., Kleitz, F., Thommes, M., 2016. Insights into the pore structure of KIT-6 and SBA-15 ordered mesoporous silica – recent advances by combining physical adsorption with mercury porosimetry. New J. Chem. 40, 4351–4360. doi:10.1039/C5NJ03466C.

[17] Guillet-Nicolas, R., Bérubé, F., Thommes, M., Janicke, M.T., Kleitz, F., 2017. Selectively tuned pore condensation and hysteresis behavior in mesoporous sba-15 silica: Correlating material synthesis to advanced gas adsorption analysis. The Journal of Physical Chemistry C 121, 24505–24526. doi:10.1021/acs.jpcc.7b06745.

[18] Halsey, G., 1948. Physical adsorption on non-uniform surfaces. The Journal of Chemical Physics 16, 931–937. doi:10.1063/1.1746689.

[19] Harkins, W.D., Jura, G., 1944. Surfaces of solids. xiii. a vapor adsorption method for the determination of the area of a solid without the assumption of a molecular area, and the areas occupied by nitrogen and other molecules on the surface of a solid. Journal of the American Chemical Society 66, 1366–1373. doi:10.1021/ja01236a048.

[20] Haul, R. S. J. Gregg, K.S.W.S., 1982. Adsorption, surface area and porosity. 2. auflage, academic press, london 1982. Berichte der Bunsengesellschaft für physikalische Chemie 86, 957–957. doi:https://doi.org/10.1002/bbpc.19820861019.

[21] He, L., Ren, X., Gao, Q., Zhao, X., Yao, B., Chao, Y., 2017. The connected-component labeling problem: A review of state-of-the-art algorithms. Pattern Recognition 70, 25 – 43. doi:https://doi.org/10.1016/j.patcog.2017.04.018.

[22] Hoshen, J., Kopelman, R., 1976. Percolation and cluster distribution. i. cluster multiple labeling technique and critical concentration algorithm. Phys. Rev. B 14, 3438–3445. doi:10.1103/PhysRevB.14.3438.

[23] Ioannidis, M.A., Chatzis, I., 1993. A mixed-percolation model of capillary hysteresis and entrapment in mercury porosimetry. Journal of Colloid and Interface Science 161, 278–291. doi:https://doi.org/10.1006/jcis.1993.1468.

[24] Jeulin, D., 2000. Random texture models for material structures. Statistics and Computing 10, 121–132. doi:10.1023/A:1008942325749.

[25] Jeulin, D., 2021. Morphological Models of Random Structures. Number 53 in Interdisciplinary Applied Mathematics, Springer International Publishing. doi:10.1007/978-3-030-75452-5.

[26] Jeulin, D., Moreaud, M., 2005. Multi-scale simulation of random spheres aggregates - application to nanocomposites. Proc. 9th European Congress on Stereology and Image Analysis 1, 341–348.

[27] Jeulin, D., Moreaud, M., 2006. Percolation d'agrégats multi-échelles de sphères et de fibres – Application aux nanocomposites, in: Matériaux 2006, Dijon, France. pp. 341–348.

[28] Kikkinides, E.S., Monson, P.A., Valiullin, R., 2020. Sorption isotherm reconstruction and extraction of pore size distributions for serially connected pore model (scpm) structures employing algorithmic and statistical models. The Journal of Physical Chemistry C 124, 21591–21607. doi:10.1021/acs.jpcc.0c06710.

[29] Kleitz, F., Liu, D., Anilkumar, G.M., Park, I.S., Solovyov, L.A., Shmakov, A.N., Ryoo, R., 2003. Large cage face-centered-cubic fm3m mesoporous silica: Synthesis and structure. The Journal of Physical Chemistry B 107, 14296–14300. doi:10.1021/jp036136b.

[30] Kolesnikov, A.L., Budkov, Y.A., Gor, G.Y., 2020. Adsorption-induced deformation of mesoporous materials with corrugated cylindrical pores. The Journal of Chemical Physics 153, 194703. doi:10.1063/5.0025473.

[31] Kolesnikov, A.L., Budkov, Y.A., Gor, G.Y., 2021. Models of adsorption-induced deformation: ordered materials and beyond. Journal of Physics: Condensed Matter 34, 063002. URL: https://doi.org/10.1088/1361-648x/ac3101, doi:10.1088/1361-648x/ac3101.

[32] Kolesnikov, A.L., Georgi, N., Budkov, Y.A., Möllmer, J., Hofmann, J., Adolphs, J., Gläser, R., 2018. Effects of enhanced flexibility and pore size distribution on adsorption-induced deformation of mesoporous materials. Langmuir 34, 7575–7584. doi:10.1021/acs.langmuir.8b00591. pMID: 29792800.

[33] König, P.M., Roth, R., Mecke, K.R., 2004. Morphological thermodynamics of fluids: Shape dependence of free energies. Phys. Rev. Lett. 93, 160601. URL: https://link.aps.org/doi/10.1103/PhysRevLett.93.160601, doi:10.1103/PhysRevLett.93.160601.

[34] Landers, J., Gor, G.Y., Neimark, A.V., 2013. Density functional theory methods for characterization of porous materials. Colloids and Surfaces A: Physicochemical and Engineering Aspects 437, 3–32. doi:https://doi.org/10.1016/j.colsurfa.2013.01.007. characterization of Porous Materials: From Angstroms to Millimeters A Collection of Selected Papers Presented at the 6th International Workshop, CPM-6 April 30 – May 2nd, 2012, Delray Beach, FL, USA Co-sponsored by Quantachrome Instruments.

[35] Ledezma, G., Verstraete, J., Sorbier, L., Cocq, D.L.L., Jolimaitre, E., Jallut, C., 2021. Computational characterization of a pore network model by using a fast nitrogen porosimetry simulation, in: Türkay, M., Gani, R. (Eds.), 31st European Symposium on Computer Aided Process Engineering. Elsevier. volume 50 of *Computer Aided Chemical Engineering*, pp. 1111–1116. doi:https://doi.org/10.1016/B978-0-323-88506-5.50171-6.

[36] Luisa Ojeda, M., Marcos Esparza, J., Campero, A., Cordero, S., Kornhauser, I., Rojas, F., 2003. On comparing BJH and NLDFT pore-size distributions determined from N2 sorption on SBA-15 substrata. Phys. Chem. Chem. Phys. 5, 1859–1866. doi:10.1039/B300821E.

[37] Matheron, G., 1967. Éléments pour une théorie des milieux poreux. Masson et Cie.

[38] Matheron, G., 1974. Random sets and integral geometry [by] G. Matheron. Wiley New York.

[39] Mecke, K., Arns, C.H., 2005. Fluids in porous media: a morphometric approach 17, S503–S534. doi:10.1088/0953-8984/17/9/014.

[40] Moreaud, M., Chaniot, J., Fournel, T., Becker, J.M., Sorbier, L., 2018. Multi-scale stochastic morphological models for 3d complex microstructures. 2018 17th Workshop on Information Optics (WIO) , 1–3.

[41] Neimark, A.V., Ravikovitch, P.I., Vishnyakov, A., 2000. Adsorption hysteresis in nanopores. Phys Rev E Stat Phys Plasmas Fluids Relat Interdiscip Topics 62, R1493–1496.

[42] Nguyen, P.T.M., Do, D.D., Nicholson, D., 2011. On the hysteresis loop of argon adsorption in cylindrical pores. The Journal of Physical Chemistry C 115, 4706–4720. doi:10.1021/jp111254j.

[43] Ohser, J., Nagel, W., Schladitz, K., 2011. The euler number of discretised sets – surprising results in three dimensions. Image Analysis Stereology 22. doi:10.5566/ias.v22.p11-19.

[44] Rasmussen, C.J., Vishnyakov, A., Thommes, M., Smarsly, B.M., Kleitz, F., Neimark, A.V., 2010. Cavitation in metastable liquid nitrogen confined to nanoscale pores. Langmuir 26, 10147–10157.

[45] Ravikovitch, P.I., Neimark, A.V., 2002. Density functional theory of adsorption in spherical cavities and pore size characterization of templated nanoporous silicas with cubic and three-dimensional hexagonal structures. Langmuir 18, 1550–1560. doi:10.1021/la0107594.

[46] Rouquerol, F., Rouquerol, J., Sing, K., 1999. Adsorption by Powders and Porous Solids. Elsevier. doi:10.1016/b978-0-12-598920-6.x5000-3.

[47] Schlumberger, C., Thommes, M., 2021. Characterization of hierarchically ordered porous materials by physisorption and mercury porosimetry—a tutorial review. Advanced Materials Interfaces 8, 2002181. doi:https://doi.org/10.1002/admi.202002181.

[48] Serra, J., 1983. Image analysis and mathematical morphology. Academic Press, Inc.

[49] Serra, J., 1986. Introduction to mathematical morphology. Computer Vision, Graphics, and Image Processing 35, 283 – 305. doi:https://doi.org/10.1016/0734-189X(86)90002-2.

[50] Thommes, M., 2010. Physical adsorption characterization of nanoporous materials. Chemie Ingenieur Technik 82, 1059–1073. doi:10.1002/cite.201000064.

[51] Thommes, M., Kaneko, K., Neimark, A.V., Olivier, J.P., Rodriguez-Reinoso, F., Rouquerol, J., Sing, K.S., 2015. Physisorption of gases, with special reference to the evaluation of surface area and pore size distribution (iupac technical report). Pure and Applied Chemistry 87, 1051 – 1069. doi:https://doi.org/10.1515/pac-2014-1117.

[52] Vishnyakov, A., Neimark, A.V., 2001. Studies of liquid vapor equilibria, criticality, and spinodal transitions in nanopores by the gauge cell monte carlo simulation method. The Journal of Physical Chemistry B 105, 7009–7020. doi:10.1021/jp003994o.

[53] Wang, H., Jeulin, D., Willot, F., Sorbier, L., Moreaud, M., 2018. Modelling of the microstructure of mesoporous alumina constrained by morphological simulation of nitrogen porosimetry. Colloids and Surfaces A: Physicochemical and Engineering Aspects 553, 378–396. doi:https://doi.org/10.1016/j.colsurfa.2018.05.043.

[54] Wang, H., Pietrasanta, A., Jeulin, D., Willot, F., Faessel, M., Sorbier, L., Moreaud, M., 2015. Modelling mesoporous alumina microstructure with 3d random models of platelets. Journal of Microscopy 260, 287–301. doi:https://doi.org/10.1111/jmi.12295.

[55] Woo, H.J., Sarkisov, L., Monson, P., 2002. Understanding adsorption hysteresis in porous glasses and other mesoporous materials, in: Rodriguez-Reinoso, F., McEnaney, B., Rouquerol, J., Unger, K. (Eds.), Characterization of Porous Solids VI. Elsevier. volume 144 of *Studies in Surface Science and Catalysis*, pp. 155–162. doi:https://doi.org/10.1016/S0167-2991(02)80129-X.

[56] Xiong, Q., Baychev, T.G., Jivkov, A.P., 2016. Review of pore network modelling of porous media: Experimental characterisations, network constructions and applications to reactive transport. Journal of Contaminant Hydrology 192, 101–117. doi:https://doi.org/10.1016/j.jconhyd.2016.07.002.

[57] Zhang, Y., Lam, F.L., Yan, Z., Hu, X., 2006. Review of Kelvin's equation and its modification in characterization of mesoporous materials. Chinese Journal of Chemical Physics 19, 102–108.

[58] Zhao, D., Feng, J., Huo, Q., Melosh, N., Fredrickson, G.H., Chmelka, B.F., Stucky, G.D., 1998. Triblock copolymer

syntheses of mesoporous silica with periodic 50 to 300 angstrom pores. Science 279, 548–552. doi:10.1126/science.279.5350.548.

[59] Štěpánek, F., Šoóš, M., Rajniak, P., 2007. Characterisation of porous media by the virtual capillary condensation method. Colloids and Surfaces A: Physicochemical and Engineering Aspects 300, 11 – 20. doi:https://doi.org/10.1016/j.colsurfa.2006.10.018.